Shidahara *et al. EJNMMI Research* 2013, **3**:32
http://www.ejnmmires.com/content/3/1/32

EJNMMI Research
a SpringerOpen Journal

ORIGINAL RESEARCH Open Access

Evaluation of the biodistribution and radiation dosimetry of the ^{18}F-labelled amyloid imaging probe [^{18}F]FACT in humans

Miho Shidahara[1,2*], Manabu Tashiro[2], Nobuyuki Okamura[3], Shozo Furumoto[3], Katsutoshi Furukawa[4], Shoichi Watanuki[2], Kotaro Hiraoka[2], Masayasu Miyake[2], Ren Iwata[5], Hajime Tamura[1], Hiroyuki Arai[4], Yukitsuka Kudo[6] and Kazuhiko Yanai[2,3]

Abstract

Background: The biodistribution and radiation dosimetry of the ^{18}F-labelled amyloid imaging probe ([^{18}F] FACT) was investigated in humans.

Methods: Six healthy subjects (three males and three females) were enrolled in this study. An average of 160.8 MBq of [^{18}F] FACT was intravenously administered, and then a series of whole-body PET scans were performed. Nineteen male and 20 female source organs, and the remainder of the body, were studied to estimate time-integrated activity coefficients. The mean absorbed dose in each target organ and the effective dose were estimated from the time-integrated activity coefficients in the source organs. Biodistribution data from [^{18}F] FACT in mice were also used to estimate absorbed doses and the effective dose in human subjects; this was compared with doses of [^{18}F] FACT estimated from human PET data.

Results: The highest mean absorbed doses estimated using human PET data were observed in the gallbladder (333 ± 251 μGy/MBq), liver (77.5 ± 14.5 μGy/MBq), small intestine (33.6 ± 30.7 μGy/MBq), upper large intestine (29.8 ± 15.0 μGy/MBq) and lower large intestine (25.2 ± 12.6 μGy/MBq). The average effective dose estimated from human PET data was 18.6 ± 3.74 μSv/MBq. The highest mean absorbed dose value estimated from the mouse data was observed in the small intestine (38.5 μGy/MBq), liver (25.5 μGy/MBq) and urinary bladder wall (43.1 μGy/MBq). The effective dose estimated from the mouse data was 14.8 μSv/MBq for [^{18}F] FACT.

Conclusions: The estimated effective dose from the human PET data indicated that the [^{18}F] FACT PET study was acceptable for clinical purposes.

Keywords: Positron emission tomography, Radiation dosimetry, Amyloid imaging, MIRD, [^{18}F] FACT

Background

Amyloid beta imaging

Deposits of amyloid β (Aβ) plaque are one of the pathological observations in patients with Alzheimer's disease (AD); Aβ deposition progresses at an earlier point than the current clinical diagnostic point for this disease [1]. For earlier diagnosis of AD and the evaluation of treatment efficacy, *in vivo* amyloid imaging using positron emission tomography (PET), which provides quantitation and visualisation of Aβ deposition in the brain, is useful. Therefore, several Aβ-binding probes dedicated for PET imaging have been developed [2,3].

Most of these PET Aβ ligands are ^{11}C-labelled compounds (physical half life ($T_{1/2}$), 20 min), and ^{18}F-labelled agents are being increasingly investigated owing to their long half life ($T_{1/2}$, 109.7 min). The long $T_{1/2}$ of ^{18}F enables several PET scans to be carried out from a single synthesis of labelled agent and also enables its commercial distribution to any PET facility. On the other hand, the longer the $T_{1/2}$ of the radioisotope gets, the greater is the radiation

* Correspondence: shidahara@med.tohoku.ac.jp
[1]Division of Medical Physics, Tohoku University School of Medicine, 2-1 Seiryo-machi, Aoba-ku, Sendai 980-8575, Japan
[2]Division of Cyclotron Nuclear Medicine, Cyclotron Radioisotope Center, Tohoku University, Sendai 980-8578, Japan
Full list of author information is available at the end of the article

dose exposure for the PET subject for the same administered dose of radioligand.

Importance of radiation dosimetry

For subjects undergoing PET, internal radiation exposure is inevitable, and the radiation dose delivered is proportional to the level of radioactivity of the injected radioligand and the number of injections. In the case of amyloid imaging, subjects often have multiple PET scans for diagnostic or therapeutic longitudinal monitoring of Aβ aggregation in the brain. Therefore, estimation of the radiation dose exposure from each PET radioligand and the use of well-balanced PET scan protocols taking into consideration subject risk and benefit are important.

Estimation of the internal radiation dose requires a time series measurement of the biodistribution of the injected radioligand. There are two ways to establish the biodistribution of a radioligand in humans: one is to extrapolate from data obtained in animal experiments [4] and the other is to use data from a clinical whole-body PET study [5]. Data extrapolated from animal experiments have been used to estimate clinical radiation dose. However, Sakata et al. reported that in some radioligands, there were considerable differences in organ dose or kinetics between human and animal experiments and that a whole-body PET study would be desirable for the initial clinical evaluation of new PET radioligands [6].

Previous biodistribution and dosimetry study for PET amyloid imaging

Recently, radiation dose exposures from several PET amyloid imaging agents have been reported using clinical whole-body PET scans. One of the popular amyloid ligands, Pittsburgh compound B ([^{11}C]PIB), has been extensively investigated with regard to its kinetics in the human body, and its effective radiation dose was found to be 4.74 μSv/MBq on average [7]. For ^{18}F-labelled PET amyloid radioligands, effective doses in humans have been reported as follows: ^{18}F-AV-45, 13 and 19.3 μSv/MBq [8,9]; ^{18}F-GE067, 33.8 μSv/MBq [10]; and ^{18}F-BAY94-9172, 14.7 μSv/MBq [11].

Aim of the present study

Fluorinated amyloid imaging compound ([^{18}F]FACT) is an ^{18}F-labelled amyloid imaging agent developed at Tohoku University [12]. Kudo and colleagues at this university have previously developed a ^{11}C amyloid imaging agent named [^{11}C]BF-227 [3]. [^{18}F]FACT is derived from [^{11}C]BF-227 by reducing its lipophilicity in order to reduce the nonspecific binding in the brain; AD patients showed significantly higher uptake of [^{18}F]FACT in the neocortex region relative to controls [12]. However, the biodistribution of [^{18}F]FACT in humans has not yet been investigated.

In the present study, the radiation dosimetry and biodistribution of [^{18}F]FACT was investigated in healthy elderly subjects who are the target group for PET amyloid imaging. In order to determine the discrepancy in the estimated radiation dose between human and animal experiments, biodistribution studies in mice involving [^{18}F]FACT were also conducted.

Methods

Subjects

PET studies were performed in three healthy male and in three healthy female volunteers (mean age ± standard deviation (SD), 76.3 ± 3.2 years). Subject characteristics are shown in Table 1. Both height and weight varied over a wide range (146 to 175 cm and 39 to 74 kg, respectively). All subjects were Japanese and were free of somatic and neuropsychiatric illness, as determined by clinical history and physical examination; one male subject (no. 1) had undergone a previous surgical operation involving gallbladder removal.

This study was approved by the Ethics Committee on Clinical Investigations of Tohoku University School of Medicine and was performed in accordance with the Declaration of Helsinki. Written informed consent was obtained from all subjects after a complete description of the study had been made.

Radiochemistry and radioligand purity

Figure 1 shows the chemical structure of ^{18}F-FACT. The radiochemical purity of the radioligand in the present clinical study ranged from 97.8% to 98.7% (mean ± SD, 98.33 ± 0.42%). The specific radioactivity ranged from 30.6 to 347.7 GBq/μmol at the time of injection (mean ± SD, 139.9 ± 116.2 GBq/μmol).

PET study

All whole-body PET studies were performed using a SET-2400W scanner (Shimadzu Inc., Kyoto, Japan) in two-dimensional (2D) mode [13]. The PET scanner acquired 63 image slices at a centre-to-centre interval of 3.125 mm and had a spatial resolution of 3.9 mm full width at half maximum (FWHM) and a *Z*-axis resolution of 6.5 mm FWHM at centre field of view [13].

An overview of scan protocols is shown in Figure 2. Four emission scans and two transmission scans (before administration and intermediate emission scans) using a ^{68}Ge/^{68}Ga source were performed, with the exception of subject no. 1 who had three emission scans. In the present series of PET studies and in other research projects, a 15-min PET brain scan using three-dimensional (3D) mode was performed after the first emission scan. At 2 min after intravenous administration of 142 to 180 MBq [^{18}F]FACT (mean ± SD, 160.8 ± 14.8 MBq; injection mass, 0.77 ± 0.66 ng), a series of whole-body PET

Table 1 Information regarding the human subjects

	Sex	Age (years)	Height (m)	Weight (kg)	BMI (kg/m^2)	History
Subject number						
1	M	77	1.59	61.2	24.2	Surgical removal of gallbladder
2	M	78	1.62	65	24.8	-
3	M	77	1.75	74	24.2	-
4	F	70	1.46	39	18.3	-
5	F	77	1.56	60.2	26.1	-
6	F	79	1.55	56	23.3	-
Mean ± 1 SD		76.3 ± 3.2	1.58 ± 0.75	59.2 ± 11.6	23.5 ± 2.7	

scans were performed. The schedule for the first and second transmission scans and the first, second, third and fourth emission scans was as follows: 6 positions × 4 min (24 min), 6 positions × 4 min (24 min), 6 positions × 3 min (18 min), 6 positions × 3 min (18 min), 6 positions × 3 min (18 min), and 6 positions × 4 min (24 min), respectively. The starting time of the second emission scan was different for each subject and was on average 55 min after the start of injection with a 5-min SD. The time gap between bed positions was 5 s. All emission data were reconstructed using OS-EM with iteration 16 and subset 2 after attenuation correction. Scatter correction was not performed because of the use of 2D mode data acquisition. The cross calibration factor of the scanner (Bq per ml/cps per voxel) was determined once per week using a cylindrical water phantom (25-cm length and 20-cm inner diameter) filled with ^{18}F solutions and by measuring the sample activity of the ^{18}F solutions at the well counter (BSS-3: Shimadzu Co., Ltd., Kyoto, Japan) [14].

Urination was controlled before, after and during the series of PET studies. In particular, during (15 min after the end of the first emission scan) and after the PET scans, subjects were asked to void. The volume and radioactivity levels of their urine samples were measured using a calibrated well counter.

MRI study

All subjects underwent T1-weighted magnetic resonance imaging (MRI) scans using a Signa 1.5-T machine (General Electric Inc., Milwaukee, WI, USA) within a week of the PET scans. For each position (brain, chest, abdomen and epigastric region), individual T1-weighted scans with a voxel size of 1.875 × 1.875 × 6.000 mm (TR = 460 ms, TE = 14 ms, image matrix = 256 × 256 × 40) were obtained with subjects holding their breath.

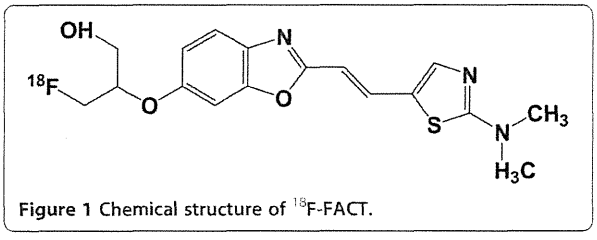

Figure 1 Chemical structure of ^{18}F-FACT.

Dosimetry

The Medical Internal Radiation Dose committee of the Society of Nuclear Medicine developed the algorithm to calculate absorbed dose D (the energy deposited per unit mass of medium (Gy)) in organs. The basic idea is that radiation energy from the radioisotope in the source organ is absorbed in the target organs, and the algorithm requires the net accumulated radioactivity in source organs as an input [15]. A PET scan contributes to quantitative knowledge on the whole-body distribution of radioisotope. In the present study, the accumulated activity in source organs was derived from PET measurements and the organ volumes of the reference male or female. The mean absorbed dose to the kth target organ is defined as follows:

$$\bar{D}(r_k) = \sum_h \tilde{A}_h \times S(r_k \leftarrow r_h) = \sum_h A_0 \times \tau_h \times S(r_k \leftarrow r_h),\ \tau_h = \frac{\tilde{A}_h}{A_0} \quad (1)$$

where $S(r_k \leftarrow r_h)$ is the absorbed dose in the kth target organ per unit of accumulated activity in the hth source organ, called the S value. $\tilde{A}_h$ is the number of disintegrations in the hth source organ, A_0 is the injected dose, and τ_h is the time-integrated activity coefficient in the hth source organ (equal to the number of disintegrations per unit activity administered). The effective dose E (Sv), as defined by the International Commission on Radiological Protection (ICRP) 60 [10], was obtained using the following equation:

$$E = \sum_i Q \times w_i \times D_i \quad (2)$$

where D_i is the absorbed dose of the ith target organ, w_i is the weighting risk factor in the ith target organ, and Q is the quality factor (Q = 1 for β- and γ-rays).

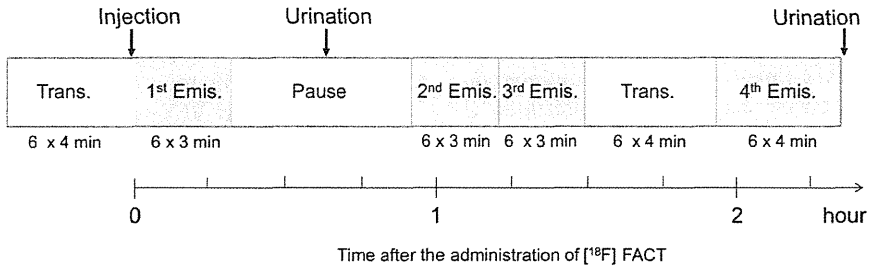

Figure 2 Overview of PET scan protocols. Four emission scans and two transmission scans (before and intermediate emission scans) with a $^{68}Ge/^{68}Ga$ source were performed. In particular, the second transmission scan was performed using a post-injection transmission scan.

Regions of interest

The number of source organs used for region-of-interest (ROI) drawing was 19 for male and 20 for female subjects. A detailed list of source organs is shown in Table 2. Two nuclear medicine physicians manually drew the ROIs using PMOD version 3.1 (PMOD Technologies, Zurich, Switzerland). All individual PET images and MRI images were co-registered to the first individual PET images using a rigid matching module of the same PMOD with a dissimilarity function of normalised mutual information (for MRI-to-PET cases) and the sum of the absolute difference (for PET-to-PET cases) algorithms.

For visceral organs with extremely high uptake (liver and gallbladder), individual ROIs were defined at a fixed

Table 2 [^{18}F]FACT time-integrated activity coefficients in the source organs

Organ	Human (MBq-h/MBq)							Mouse (MBq-h/MBq)
	Mean ± 1 SD	Subject 1	Subject 2	Subject 3	Subject 4	Subject 5	Subject 6	
Adrenal gland	5.38E−04 ± 2.98E−04	9.40E−04	8.40E−04	5.20E−04	3.70E−04	4.00E−04	1.60E−04	-
Brain	4.20E−02 ± 8.44E−03	5.41E−02	3.68E−02	3.53E−02	4.87E−02	4.42E−02	3.26E−02	6.99E−03
Breast	8.40E−03 ± 4.37E−03	1.14E−03	8.25E−03	5.59E−03	1.16E−02	1.19E−02	1.19E−02	-
Gallbladder content[a]	2.22E−01 ± 1.05E−01	-	1.49E−01	2.27E−01	3.88E−01	1.16E−01	2.31E−01	-
Lower large intestine content	2.12E−02 ± 2.03E−02	5.91E−02	1.06E−02	4.80E−03	2.27E−02	2.40E−02	5.96E−03	-
Small intestine content	8.78E−02 ± 1.08E−01	7.40E−02	3.74E−02	3.34E−02	3.06E−01	3.36E−02	4.25E−02	1.22E−01
Stomach content	6.71E−03 ± 2.28E−03	5.22E−03	6.23E−03	9.29E−03	9.84E−03	4.78E−03	4.87E−03	-
Upper large intestine content	2.55E−02 ± 1.89E−02	1.48E−02	4.88E−02	1.01E−02	4.99E−02	2.04E−02	8.85E−03	-
Heart content	1.12.E−02 ± 1.51E−03	1.24E−02	1.13E−02	1.02E−02	1.30E−02	1.15E−02	8.83E−03	3.95E−03
Heart wall	7.50E−03 ± 1.84E−03	4.63E−03	1.00E−02	8.84E−03	6.75E−03	7.28E−03	7.49E−03	2.39E−03
Kidney	1.34E−02 ± 3.27E−03	1.32E−02	1.16E−02	1.53E−02	1.89E−02	9.59E−03	1.20E−02	9.34E−03
Liver	4.92E−01 ± 1.05E−01	6.28E−01	5.85E−01	4.34E−01	5.15E−01	3.42E−01	4.49E−01	1.69E−01
Lung	3.55E−02 ± 1.16E−02	3.78E−02	5.31E−02	4.36E−02	2.46E−02	2.33E−02	3.08E−02	1.17E−02
Muscle	4.66E−01 ± 3.73E−01	9.43E−01	5.47E−01	7.97E−01	5.40E−02	4.12E−01	4.34E−02	1.57E−01
Ovary[b]	5.53E−04 ± 3.79E−05	-	-	-	5.70E−04	5.10E−04	5.80E−04	-
Pancreas	4.13E−03 ± 9.75E−04	6.10E−03	3.62E−03	3.93E−03	3.81E−03	3.55E−03	3.76E−03	-
Red marrow	3.98E−02 ± 4.33E−03	4.02E−02	3.83E−02	3.79E−02	4.59E−02	4.29E−02	3.34E−02	1.61E−02
Spleen	5.41E−03 ± 1.74E−03	8.64E−03	4.88E−03	3.83E−03	6.01E−03	4.77E−03	4.30E−03	1.28E−03
Testis[c]	5.77E−04 ± 4.67E−04	7.00E−04	6.10E−05	9.70E−04	-	-	-	-
Thyroid	3.53E−04 ± 1.55E−04	6.30E−04	3.70E−04	3.60E−04	2.40E−04	1.80E−04	3.40E−04	-
Urinary bladder contents	2.26E−02 ± 8.36E−03	1.70E−02	2.69E−02	1.55E−02	3.63E−02	2.49E−02	1.51E−02	6.56E−02
Uterus/uterine wall[b]	4.46E−03 ± 1.90E−03	-	-	-	6.42E−03	2.63E−03	4.33E−03	-
Remainder of the body	1.17 ± 3.63E−01	7.24E−01	1.06	9.48E−01	1.08	1.51	1.69	2.08

Averaged time-integrated activity coefficient (MBq-h/MBq) for the source organs (n = 6) from the whole-body PET data (n = 6) from experiments involving human subjects of [^{18}F]FACT and mice of [^{18}F]FACT. [a]Averaged value among five subjects excluding subject no. 1. [b]Average time-integrated activity coefficient among female subjects (n = 3). [c]Average time-integrated activity coefficient among male subjects (n = 3).

emission scan with about a 40% threshold against the maximum counts (first emission for the liver and third or fourth emission for the gallbladder). Then the ROI was applied to the other emission images with minor adjustment of its location or shape. For the intestines, if specific high uptake was observed, individual ROIs were defined on each time frame of the PET images with about a 10% threshold. If there was no specific high uptake in the intestines, and uptake could be regarded as uniform, individual ROIs were drawn around the corresponding area.

In order to obtain a typical radioactivity concentration within organs with less location mismatch between PET and the co-registered MRI images (brain, breast, heart wall, heart contents, kidney, liver, lung, muscle, bones, spleen and thyroid), individual ROIs were drawn on co-registered MRI images. For other low-uptake organs (adrenal gland, stomach contents, pancreas, ovary, uterus and testis), individual ROIs were drawn on each time frame of the PET images and referred to the co-registered MRI images. To avoid a partial volume effect, the size of the ROI for these MRI available organs was made slightly smaller than the entire source organ. It should also be noted that all activities in vertebrae ROIs was assumed to be in the red marrow in the present study.

Data analysis

Averaged time-activity curves for each organ were obtained using the ROI values from each subject's PET images. Because the PET images were decay-corrected at the start of each scan during the reconstruction procedure, the non-decay-corrected time-activity curves (C(t), Bq/ml) were re-calculated. During each whole-body emission scan, the bed position was moved from the foot to the head (six bed positions in total). However, we assumed that PET counts at all bed positions were acquired at the mid-scan time. Then, individual radioactivity concentration per injected dose A_0 (Bq) was extrapolated into the percent injected dose (%ID) of the reference subject as follows:

$$\%\mathrm{ID}(t)_{\mathrm{reference}} = \left(\frac{C(t)}{A_0}\right)_{\mathrm{individual}} \times V_{\mathrm{reference}} \qquad (3)$$

where V (ml) is the organ volume, and $V_{\mathrm{reference}}$ is V of the reference subject (we used a 70-kg adult male and 58-kg adult female as the male and female reference subjects) [16,17]. Even though some organs such as the intestine may change their volume over time, we used the reference subjects' organ volumes over the time period of the calculation of the %ID.

The time-integrated activity coefficient τ (Bq-h/Bq) in Equation 1 was obtained by fitting (%ID(t)) using a mono-exponential function and integrating from time zero to infinity. If the time-activity curve did not converge at the last PET scan (e.g. intestines and gallbladder), time-activity curves were fitted using two exponential functions, and then the area under the curve after the acquisition of the last image was calculated by assuming only physical decay of ^{18}F and no additional biologic clearance to be conservative [10]. The time-integrated activity coefficient for urinary bladder content was calculated by applying the dynamic urinary bladder model [10] to the urine samples with a bladder voiding interval of 2 h. The decay-corrected cumulative activity for urine was fitted using the equation $A \times (1 - \exp(-\ln(2) \times t / \tau))$, where τ is the biological decay and A is the fraction of activity released from the body. The sum of the time-integrated activity coefficient for the specific organs was subtracted from the time-integrated activity coefficient for the total body, which was calculated from the time integral of the decaying injected radioactivity. Then the residual of the subtraction was regarded as the time-integrated activity coefficient in the remainder of the body. All fitting procedures were undertaken using a mean fit of R^2 of 0.93 ± 0.13.

Finally, the time-integrated activity coefficient τ (Bq-h/Bq) was used to calculate the absorbed dose, D, in Equation 1 and the effective dose, E, in Equation 2. Both kinetics calculations (fitting and integration) and dose estimation were performed using OLINDA/EXM software version 1.0 (Department of Radiology and Radiological Sciences Vanderbilt University, Nashville, TN, USA) [17].

Animal experiments

The experimental protocols were reviewed by the Committee on the Ethics of Animal Experiments at Tohoku University School of Medicine and performed in accordance with the Guidelines for Animal Experiments issued by the Tohoku University School of Medicine. Estimated radiation dose of [^{18}F]FACT in the human subjects calculated from mouse data sets was compared with those of [^{18}F]FACT from human whole-body PET scans. An average dose of 1.4 MBq of [^{18}F]FACT was intravenously injected into ICR mice (age, 6 weeks; average body weight, 30 g) without anaesthesia. In the [^{18}F]FACT study, the mice were killed by cervical luxation at 2, 10, 30, 60 and 120 min ([^{18}F]FACT) after administration (n = 4 at each time point). The masses of the blood, heart, lung, liver, spleen, small intestine, kidney, brain and urine samples were measured, and activity was also measured using a well counter. Thigh bone and muscle were also sampled. The average uptake of the

radioligand into the male reference subject (70 kg) was extrapolated as follows [18]:

$$\%\mathrm{ID}(t)_{\mathrm{human}} = \left(\frac{\%\mathrm{ID}(t)}{\mathrm{mass}_{\mathrm{organ}}}\right)_{\mathrm{mouse}} \times \left(\mathrm{mass}_{\mathrm{body}}\right)_{\mathrm{mouse}} \times \left(\frac{\mathrm{mass}_{\mathrm{organ}}}{\mathrm{mass}_{\mathrm{body}}}\right)_{\mathrm{human}} \quad (4)$$

where the bodyweight of the mouse was assumed to be 30 for [^{18}F]FACT.

Finally, in the same manner as in the human PET data analysis, time-integrated activity coefficients, absorbed doses and effective doses were calculated using the OLINDA/EXM software version 1.0. Sampled blood, thighbone and urine were regarded as heart contents, red bone marrow and urinary bladder contents, respectively.

Results and discussion

Biodistribution of [^{18}F]FACT

Figure 3A is the coronal PET image for a single female subject (no. 5) and demonstrates the typical biodistribution of [^{18}F]FACT in the human body. The highest accumulations of this radioligand were observed in the gallbladder, liver, intestine and urinary bladder. For subject no. 1, [^{18}F]FACT contained in the bile was excreted from the liver to the duodenum through the biliary tract (Figure 3B). The biodistribution pattern of [^{18}F]FACT in human subjects showed a predominant hepatobiliary excretion, which is similar to what has been observed for other amyloid ligands, such as [^{11}C]PIB, [^{18}F]AV-45, [^{18}F]GE067 and [^{18}F]BAY94-9172 [7,8,10,11].

Figure 4 shows the decay-corrected time-activity curve of the %ID for typical source organs (brain, liver, spleen, lung, kidney, heart content, heart wall, muscle, red marrow, small intestine contents, gallbladder, upper large intestine contents and urinary bladder) from the six volunteers and the mice experiments. A significant difference between the %ID from humans and mice was observed in the brain, liver, spleen, heart contents, red marrow and urinary bladder, and these differences propagated the different results regarding dose estimation. In human subjects, ^{18}F uptake in the gallbladder contents and the intestines (Figure 4J,K,L) indicated larger individual variations in radioactivity uptake relative to other organs (e.g. the kidney as shown in Figure 4E). Radioactivity uptake in the upper large intestine showed propagation of both ligand kinetics and inter-subject variation from the gallbladder (Figure 4K,L). Scheinin et al. previously reported that inter-subject variation in ligand uptake ([^{11}C]PIB) in the gallbladder may be due to the quality and quantity of post-injection food intake [7]. In the present study, the subjects drank water during the interval between the first and second PET scans. This may have been responsible for the increase in inter-subject variation regarding the gallbladder. Furthermore, because the gallbladder uptake in some subjects had declined or remained at a low level at the final time points, we assumed that there was only physical radioactive decay after the last PET scans. However, this assumption may have led to a conservative estimation of the absorbed dose.

Figure 5 presents typical brain PET images obtained using [^{18}F]FACT at different time points with an

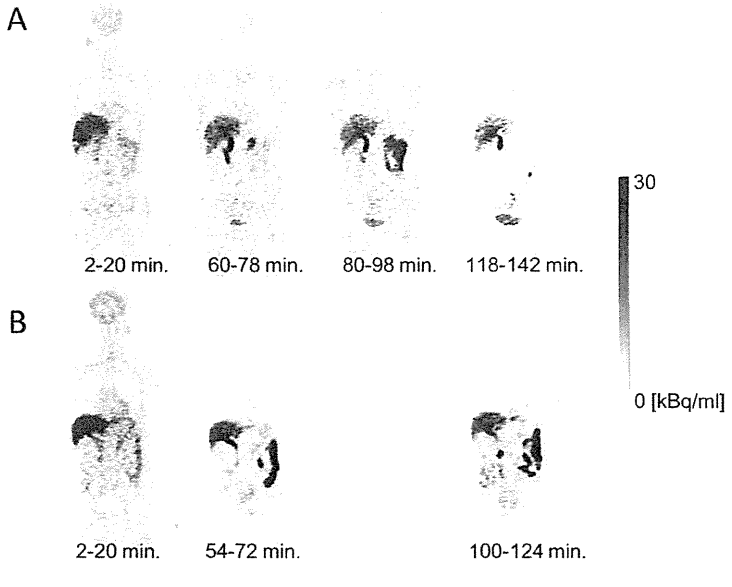

Figure 3 Decay-corrected coronal radioactivity distributions. Subject no. 5 (**A**) and subject no. 1 (**B**) at each PET measurement.

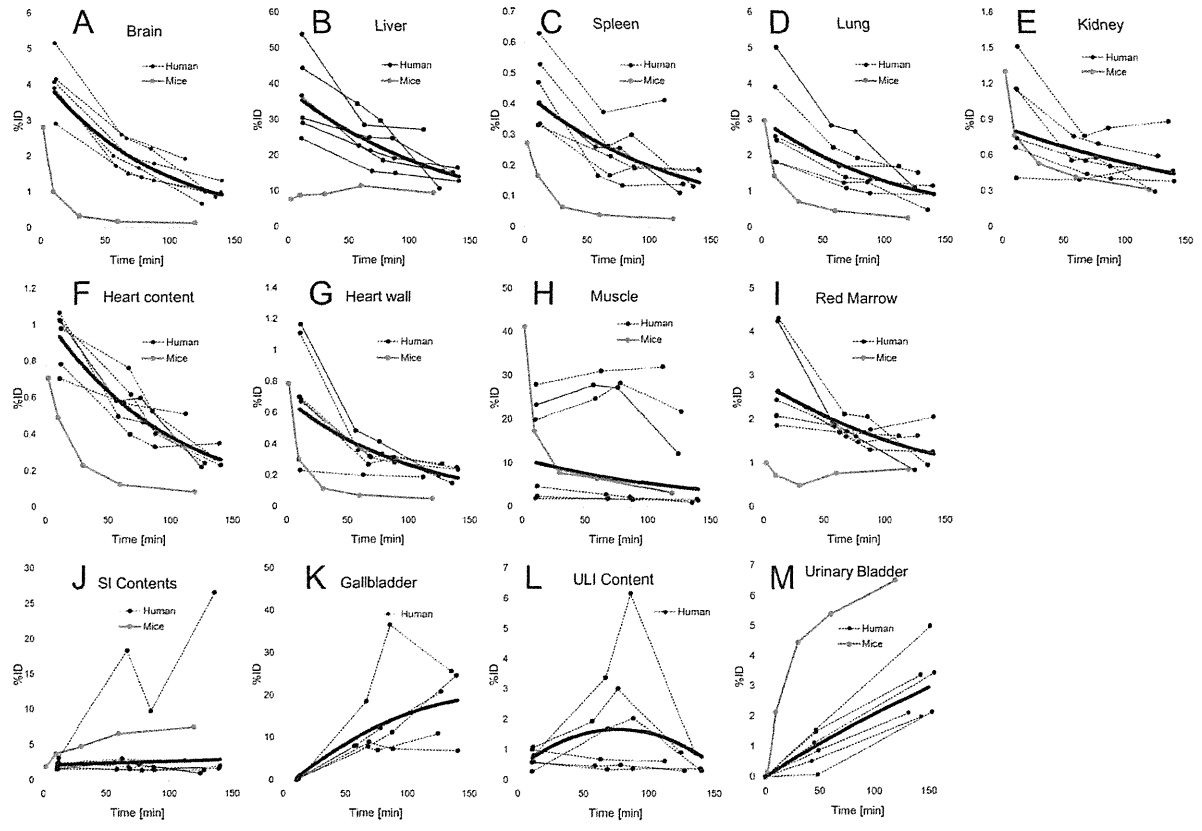

Figure 4 Decay-corrected time-activity curves of %ID. (**A**) Brain, (**B**) liver, (**C**) spleen, (**D**) lung, (**E**) kidney, (**F**) heart content, (**G**) heart wall, (**H**) muscle, (**I**) red marrow, (**J**) SI contents, (**K**) gallbladder, (**L**) ULI content and (**M**) urinary bladder for individual human (dashed black line) and averaged mice extrapolation (n = 4 at each time point, grey line). The solid black line indicates fitted curve using exponential function from all subjects' data points. The urinary bladder curve indicates accumulated activity excreted at all voiding/sampling moments.

acquisition time of 3 min (first, second and third emission) and 4 min (fourth emission). There was no significant retention of [^{18}F]FACT in the brain, and this may have been because the subject was normal.

Estimated dose of [^{18}F]FACT

The [^{18}F]FACT time-integrated activity coefficients in the source organs are shown in Table 2, and the absorbed doses are shown in Table 3. The averaged time-integrated activity coefficient for the gallbladder, as shown in Table 2, was calculated among five subjects excluding subject no. 1; however, in the case of the averaged absorbed and effective doses, subject no. 1 was included (Table 3).

High absorbed dose in humans was observed in the gallbladder (333 ± 251 μGy/MBq), liver (77.5 ± 14.5 μGy/MBq), small intestine (33.6 ± 30.7 μGy/MBq), upper large intestine (29.8 ± 15.0 μGy/MBq) and lower large intestine (25.2 ± 12.6 μGy/MBq). In mice, high absorbed doses were observed in the small intestine (38.5 μGy/MBq), liver (25.5 μGy/MBq) and urinary bladder wall (43.1 μGy/MBq) for [^{18}F]FACT (Table 3).

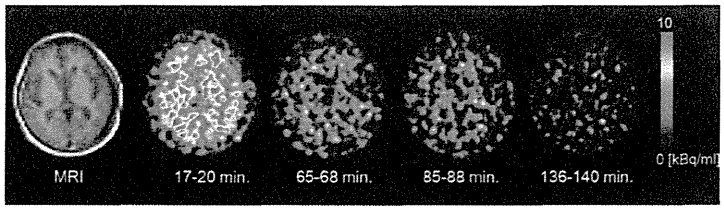

Figure 5 Decay-corrected brain PET images of subject no. 3 at different time points.

Table 3 Absorbed doses in the source organs

	Human			Mouse
	All subjects (n = 6)	Male (n = 3)	Female (n = 3)	
Organ				
Adrenal gland	1.96E01 ± 2.00	2.03E01	1.90E01	1.35E01
Brain	9.91 ± 1.82	8.95	1.09E01	4.17
Breasts	8.69 ± 2.55	6.68	1.07E01	9.90
Gallbladder wall	3.33E02 ± 2.51E02	2.16E02	4.50E02	1.68E01
Lower large intestine wall	2.52E01 ± 1.26E01	2.41E01	2.63E01	1.57E01
Small intestine	3.36E01 ± 3.07E01	2.07E01	4.64.E01	3.85E01
Stomach wall	1.61E01 ± 3.44	1.35E01	1.87E01	1.39E01
Upper large intestine wall	2.98E01 ± 1.50E01	2.36E01	3.59E01	1.83E01
Heart wall	1.62E01 ± 1.70	1.50E01	1.74E01	8.34
Kidneys	2.01E01 ± 4.30	1.85E01	2.17E01	1.32E01
Liver	7.75E01 ± 1.45E01	7.38E01	8.11E01	2.55E01
Lungs	1.46E01 ± 1.10	1.49E01	1.43E01	7.96
Muscle	1.03E01 ± 1.27	1.07E01	9.90	7.89
Ovary	1.67E01 ± 6.65	1.18E01	2.16E01	1.67E01
Pancreas	2.32E01 ± 3.11	2.17E01	2.47E01	1.45E01
Red marrow	1.31E01 ± 1.70	1.16E01	1.46E01	1.23E01
Osteogenic cells	1.60E01 ± 3.65	1.25E01	1.95E01	1.82E01
Skin	7.30 ± 1.39	5.99	8.60	8.70
Spleen	1.37E01 ± 2.48	1.27E01	1.48E01	7.83
Testis	7.32 ± 2.16	7.32	-	1.15E01
Thymus	1.00E01 ± 1.85	8.37	1.16E01	1.08E01
Thyroid	8.36 ± 1.38	8.86	7.86	1.10E01
Urinary bladder wall	2.23E01 ± 7.33	1.81E01	2.66E01	4.31E01
Uterus	1.67E01 ± 8.13	1.14E01	2.19E01	1.77E01
Total body	1.38E01 ± 1.63	1.22E01	1.53E01	1.22E01
Effective dose (μSv/MBq)	1.86E01 ± 3.74	1.64E01	2.09E01	1.48E01

Averaged absorbed dose estimates (μGy/MBq) for the target organs from the whole-body PET data (n = 6) from experiments involving human subjects of [^{18}F]FACT and mice of [^{18}F]FACT. Average absorbed dose for male subjects (n = 3).

The effective dose estimated from the human PET study was 18.6 ± 3.74 μSv/MBq. The effective doses of [^{18}F]FACT estimated from the clinical PET studies among other ^{18}F-labelled PET amyloid radioligands were as follows: [^{18}F]AV-45, 13 and 19.3 μSv/MBq [8,9]; [^{18}F]GE067, 33.8 μSv/MBq [10]; and [^{18}F]BAY94-9172, 14.67 μSv/MBq [11]. For PET analysis of [^{11}C]PIB, Scheinin et al. normalised the %ID using the ratio of individual and reference subjects' body weights (Equation 4) [7]. However, in the present study, we did not normalise the %ID data because there was a small difference between the effective dose with normalisation (17.6 ± 2.12 μSv/MBq) and the present effective dose (18.6 ± 3.74 μSv/MBq). Therefore, we concluded that body weight normalisation does not influence the effective dose.

The effective dose of [^{18}F]FACT from the mouse experiments (14.8 μSv/MBq) was underestimated as compared with that from the human subject PET studies (18.6 μSv/MBq) (Table 3). This discrepancy corresponded to 0.76 mSv (2.96 and 3.72 mSv from mice and humans, respectively) while assuming an injected activity of 200 MBq as a clinically relevant dose. The underestimation of absorbed dose in the mouse gallbladder (20 times lower) and liver (3 times lower) relative to the human PET studies may have been responsible for the underestimation of the effective dose. High absorbed doses in the liver, gallbladder and small intestine of mice indicated that the biodistribution pattern of [^{18}F]FACT in mice includes hepatobiliary excretion, as was observed in the PET scans involving human subjects. However,

the estimated absorbed dose in the gallbladder was 20 times lower than the estimate from human subject data sets because we could not remove the gallbladder of the mouse. Therefore, to evaluate the effective dose of [^{18}F]FACT in target organs, a whole-body PET scan of human subjects may be preferable as compared with the extrapolation from mouse experiments.

Clinical applicability of [^{18}F]FACT

The present whole-body PET study was performed using healthy elderly subjects and not patients with AD. Previously, Koole et al. speculated that if brain uptake of ^{18}F amyloid ligand increased by a factor of three, this will only influence estimation of the effective dose within 1%; however, when the subject had taken medication that changed the function of the hepatic metabolism, the estimated effective dose will vary with a larger range [10].

In the present series of PET studies, brain PET scans using the 3D mode were performed between the first and the second emission scan. Therefore, the injected dose for 2D whole-body scans was set to lower level than usual, and the averaged injected activity of 160.8 MBq corresponded to a radiation dose of 2.99 mSv per single administration. With regard to the optimal injected activity that can ensure sufficient image quality for clinical use, the peak noise-equivalent counts ratio (NECR) is often used in its determination. It has also been reported that the peak NECR in 2D mode was not reached with an acceptable range of injected activity, whereas in 3D mode, there was a distinct maximum for the NECR for which the corresponding injected activity was based on patient height and weight [19]. For the scanner used in our study, the NECR peak in 3D mode was reached at 4.44 kBq/ml using an 8,000-ml phantom [13]. When the subject's height and weight were assumed to be 170 cm and 60 kg, respectively, this assumption corresponded to the optimal injected dose of about 260 MBq. In a real situation, there exists the effect of the activity outside the axial FOV, and the optimal injected dose would be much lower. Injected activity indicates radiation dose; for example, 200 MBq indicates a radiation dose of 3.72 mSv. ICRP 62 [20] recommended that the maximum radiation dose that causes a 'minor to intermediate' increase of risk levels while preserving social benefit levels that are 'intermediate to moderate' has an effective limit of 10 mSv/year [20,21]. Thus, the maximum injectable activity is 537.6 MBq [^{18}F]FACT/year, and this injection dose limit allows two or three PET scans to be performed. Furthermore, amyloid imaging is mainly undertaken in elderly patients aged >50 years, even though for early detection of AD, patients aged <50 years will also have an amyloid PET scan. According to the guidance on medical exposures in medical and biomedical research by the European Commission [22], dose restrictions for patients aged over >50 years are not as strict as for younger patients. Therefore, considerably more multiple PET scans may be possible.

Conclusions

The effective dose of the ^{18}F-labelled amyloid imaging agent, [^{18}F]FACT, was found to be acceptable for clinical study.

Competing interests

The authors declare that they have no competing interests.

Authors' contributions

MS carried out the data analysis and interpretation and drafted the manuscript. TM, HT, YK and KY performed the study design and contributed to the intellectual discussion. NO, SF and RI performed the animal experiments and synthesis of PET probes. KF, SW, KH, MM and HA provided the clinical data. All authors read and approved the final manuscript.

Acknowledgements

We would like to thank Dr. Muneyuki Sakata from the Positron Medical Center, Tokyo Metropolitan Institute of Gerontology, and Dr. Hiroshi Watabe from the Cyclotron Radioisotope Center, Tohoku University, for their helpful advice regarding data analysis. This study was supported in part by Grants-in-Aid of Young Scientists (B) (no. 24700445) from the Ministry of Education, Culture, Sports, Science and Technology (MEXT), Japanese Government.

Author details

[1]Division of Medical Physics, Tohoku University School of Medicine, 2-1 Seiryo-machi, Aoba-ku, Sendai 980-8575, Japan. [2]Division of Cyclotron Nuclear Medicine, Cyclotron Radioisotope Center, Tohoku University, Sendai 980-8578, Japan. [3]Department of Pharmacology, Tohoku University School of Medicine, Sendai 980-8575, Japan. [4]Department of Geriatrics and Gerontology, Division of Brain Sciences, Institute of Development, Aging and Cancer, Tohoku University, Sendai 980-8575, Japan. [5]Division of Radiopharmaceutical Chemistry, Cyclotron Radioisotope Center, Tohoku University, Sendai 980-8578, Japan. [6]Clinical Research, Innovation and Education Center, Tohoku University Hospital, Sendai 980-8574, Japan.

Received: 23 January 2013 Accepted: 8 April 2013
Published: 24 April 2013

References

1. Hardy J, Selkoe DJ: **The amyloid hypothesis of Alzheimer's disease: progress and problems on the road to therapeutics.** *Science* 2002, 297:353–356.
2. Furumoto S, Okamura N, Iwata R, Yanai K, Arai H, Kudo Y: **Recent advances in the development of amyloid imaging agents.** *Curr Top Med Chem* 2007, 7:1773–1789.
3. Kudo Y, Okamura N, Furumoto S, Tashiro M, Furukawa K, Maruyama M, Itoh M, Iwata R, Yanai K, Arai H: **2-(2-[2-Dimethylaminothiazol-5-yl]ethenyl)-6-(2-[fluoro]ethoxy)benzoxazole: a novel PET agent for in vivo detection of dense amyloid plaques in Alzheimer's disease patients.** *J Nucl Med* 2007, 48:553–561.
4. Sakata M, Wu J, Toyohara J, Oda K, Ishikawa M, Ishii K, Hashimoto K, Ishiwata K: **Biodistribution and radiation dosimetry of the alpha7 nicotinic acetylcholine receptor ligand [^{11}C]CHIBA-1001 in humans.** *Nucl Med Biol* 2011, 38:443–448.
5. Deloar HM, Fujiwara T, Shidahara M, Nakamura T, Watabe H, Narita Y, Itoh M, Miyake M, Watanuki S: **Estimation of absorbed dose for 2-[F-18]fluoro-2-deoxy-D-glucose using whole-body positron emission tomography and magnetic resonance imaging.** *Eur J Nucl Med Mol Imaging* 1998, 25:565–574.
6. Sakata M, Oda K, Toyohara J, Ishii K, Nariai T, Ishiwata K: **Direct comparison of radiation dosimetry of six PET tracers using human whole-body imaging and murine biodistribution studies.** *Ann Nucl Med* 2013, 27:285–296.
7. Scheinin NM, Tolvanen TK, Wilson IA, Arponen EM, Nagren KA, Rinne JO: **Biodistribution and radiation dosimetry of the amyloid imaging agent ^{11}C-PIB in humans.** *J Nucl Med* 2007, 48:128–133.

8. Lin KJ, Hsu WC, Hsiao IT, Wey SP, Jin LW, Skovronsky D, Wai YY, Chang HP, Lo CW, Yao CH, Yen TC, Kung MP: **Whole-body biodistribution and brain PET imaging with [^{18}F]AV-45, a novel amyloid imaging agent–a pilot study.** *Nucl Med Biol* 2010, **37**:497–508.
9. Wong DF, Rosenberg PB, Zhou Y, Kumar A, Raymont V, Ravert HT, Dannals RF, Nandi A, Brasic JR, Ye W, Hilton J, Lyketsos C, Kung HF, Joshi AD, Skovronsky DM, Pontecorvo MJ: **In vivo imaging of amyloid deposition in Alzheimer disease using the radioligand ^{18}F-AV-45 (florbetapir [corrected] F 18).** *J Nucl Med* 2010, **51**:913–920.
10. Koole M, Lewis DM, Buckley C, Nelissen N, Vandenbulcke M, Brooks DJ, Vandenberghe R, Van Laere K: **Whole-body biodistribution and radiation dosimetry of ^{18}F-GE067: a radioligand for in vivo brain amyloid imaging.** *J Nucl Med* 2009, **50**:818–822.
11. O'Keefe GJ, Saunder TH, Ng S, Ackerman U, Tochon-Danguy HJ, Chan JG, Gong S, Dyrks T, Lindemann S, Holl G, Dinkelborg L, Villemagne V, Rowe CC: **Radiation dosimetry of beta-amyloid tracers ^{11}C-PiB and ^{18}F-BAY94-9172.** *J Nucl Med* 2009, **50**:309–315.
12. Furumoto S, Okamura N, Furukawa K, Tashiro M, Ishikawa Y, Sugi K, Tomita N, Waragai M, Harada R, Tago T, Iwata R, Yanai K, Arai H, Kudo Y: **A ^{18}F-labeled BF-227 derivative as a potential radioligand for imaging dense amyloid plaques by positron emission tomography.** *Mol Img Biol.* in press.
13. Fujiwara T, Watanuki S, Yamamoto S, Miyake M, Seo S, Itoh M, Ishii K, Orihara H, Fukuda H, Satoh T, Kitamura K, Tanaka K, Takahashi S: **Performance evaluation of a large axial field-of-view PET scanner: SET-2400W.** *Ann Nucl Med* 1997, **11**:307–313.
14. Watanuki S, Tashiro M, Miyake M, Ishikawa Y, Itoh M, Yanai K, Sakemi Y, Fukuda H, Ishii K: **Long-term performance evaluation of positron emission tomography: analysis and proposal of a maintenance protocol for long-term utilization.** *Ann Nucl Med* 2010, **24**:461–468.
15. Loevinger R, Budinger T, Watson E: *MIRD Primer for Absorbed Dose Calculations. Revised edn.* New York: The Society of Nuclear Medicine; 1991.
16. Cristy M, Eckerman KF: *Specific Absorbed Fractions of Energy at Various Ages from Internal Photon ources.* Oak Ridge: ORNL/TM; 1987:8381.
17. Stabin MG, Sparks RB, Crowe E: **OLINDA/EXM: the second-generation personal computer software for internal dose assessment in nuclear medicine.** *J Nucl Med* 2005, **46**:1023–1027.
18. Kirschner AS, Ice RD, Beierwaltes WH: **Radiation dosimetry of ^{131}I-19-iodocholesterol: the pitfalls of using tissue concentration data -reply.** *J Nucl Med* 1975, **16**:248–249.
19. Lartizien C, Comtat C, Kinahan PE, Ferreira N, Bendriem B, Trebossen R: **Optimization of injected dose based on noise equivalent count rates for 2- and 3-dimensional whole-body PET.** *J Nucl Med* 2002, **43**:1268–1278.
20. ICRP: *Radiological Protection in Biomedical Research.* Oxford: Pergamon; 1992.
21. Kimura Y, Simeon FG, Hatazawa J, Mozley PD, Pike VW, Innis RB, Fujita M: **Biodistribution and radiation dosimetry of a positron emission tomographic ligand, ^{18}F-SP203, to image metabotropic glutamate subtype 5 receptors in humans.** *Eur J Nucl Med Mol Imaging* 2010, **37**:1943–1949.
22. Directorate-General Environment NSaCP: **Guidance on medical exposures in medical and biomedical research.** In *Radiation Protection.* Brussels: European Commission; 1998:1–14.

doi:10.1186/2191-219X-3-32
Cite this article as: Shidahara *et al.*: Evaluation of the biodistribution and radiation dosimetry of the ^{18}F-labelled amyloid imaging probe [^{18}F] FACT in humans. *EJNMMI Research* 2013 **3**:32.

MOLECULAR IMAGING AND BIOLOGY

Mol Imaging Biol (2013)
DOI: 10.1007/s11307-012-0608-5

World Molecular Imaging Society

RESEARCH ARTICLE

A ^{18}F-Labeled BF-227 Derivative as a Potential Radioligand for Imaging Dense Amyloid Plaques by Positron Emission Tomography

Shozo Furumoto,[1,2] Nobuyuki Okamura,[1] Katsutoshi Furukawa,[3] Manabu Tashiro,[4] Yoichi Ishikawa,[2] Kentaro Sugi,[1] Naoki Tomita,[3] Masaaki Waragai,[3] Ryuichi Harada,[1] Tetsuro Tago,[2] Ren Iwata,[2] Kazuhiko Yanai,[1] Hiroyuki Arai,[3] Yukitsuka Kudo[5]

[1]*Department of Pharmacology, Tohoku University School of Medicine, 2-1 Seiryo-machi, Aoba-ku, Sendai 980-8575, Japan*
[2]*Division of Radiopharmaceutical Chemistry, Cyclotron and Radioisotope Center, Tohoku University, Sendai, Japan*
[3]*Department of Geriatrics and Gerontology, Division of Brain Sciences, Institute of Development, Aging and Cancer, Tohoku University, Sendai, Japan*
[4]*Division of Cyclotron Nuclear Medicine, Cyclotron and Radioisotope Center, Tohoku University, Sendai, Japan*
[5]*Clinical Research, Innovation and Education Center, Tohoku University Hospital, Sendai, Japan*

Abstract

Purpose: The aims of this study were to evaluate the binding and pharmacokinetics of novel ^{18}F-labeled ethenyl-benzoxazole derivatives (i.e., [^{18}F] fluorinated amyloid imaging compound of Tohoku university ([^{18}F]FACT)) as amyloid positron emission tomography (PET) tracers and to assess [^{18}F]FACT efficacy in imaging of Alzheimer's disease (AD).

Procedures: Binding assay was conducted using synthetic amyloid-β (Aβ) fibrils, fluorescence microscopy, and autoradiogram in three postmortem AD brains. Pharmacokinetics of [^{18}F]FACT was assessed using 12 Crj:CD-1 (ICR) mice. *In vivo* binding ability with brain amyloid was investigated using amyloid precursor protein (APP) transgenic mouse. Clinical PET scanning using [^{18}F]FACT was performed in ten healthy controls and ten mild cognitive impairment and ten AD patients.

Results: [^{18}F]FACT showed high binding affinity for synthetic Aβ fibrils, preferential binding to dense cored plaques in brain sections, and excellent brain uptake and rapid clearance in mice. Injection in APP mice resulted in specific *in vivo* labeling of amyloid deposits in the brain. PET scans of AD patients showed significantly higher [^{18}F]FACT uptake in the neocortex compared to controls ($P<0.05$, Kruskal–Wallis test).

Conclusion: [^{18}F]FACT is a promising agent for imaging dense Aβ plaques in AD.

Key words: Alzheimer's disease, Amyloid, Early diagnosis, Positron emission tomography

Introduction

Alzheimer's disease (AD) is an age-dependent and irreversible neurodegenerative disorder leading to deterioration of memory and cognitive function. Although the exact mechanisms underlying pathogenesis of AD are not fully understood, formation of brain amyloid plaques through aggregation and deposition of amyloid-β protein (Aβ) is considered to be the initial pathogenic event that may precede the appearance of clinical AD symptoms by decades. Recently, new criteria for diagnosing AD were proposed by the National Institute on Aging—Alzheimer's Association workgroups [1]. The new diagnostic criteria include the use of biomarkers for amyloid deposition to aid

Correspondence to: Nobuyuki Okamura; *e-mail:* nookamura@med.tohoku.ac.jp

Published online: 30 January 2013

in diagnosis of AD. Thus, *in vivo* detection of amyloid depositions with positron emission tomography (PET) has received much attention as a potential technology for early or presymptomatic diagnosis of AD. For this purpose, a number of radiotracers for Aβ aggregates have been synthesized and evaluated as candidates for PET amyloid imaging agents, and some of these are undergoing clinical investigation [2–4].

Among them, *N*-methyl-[^{11}C]-2-(4′-methylaminophenyl)-6-hydroxybenzothiazole ([^{11}C]Pittsburgh compound B, [^{11}C]PiB) is currently the most widely used in clinical research [5]. Labeling of PET tracers with ^{18}F ($T_{1/2}$= 109.8 min) allows time for their delivery to numerous PET centers and contributes to spreading their use. Several ^{18}F-labeled amyloid PET tracers, including [^{18}F]flutemetamol, [^{18}F]florbetaben, [^{18}F]florbetapir, and [^{18}F]AZD4694, have been developed, and to date, [^{18}F]florbetapir has become commercially available [6–9]. An increasing number of PET studies in humans have clearly demonstrated that amyloid PET is a potentially useful technique to visualize and quantify the distribution of Aβ plaques of AD patients [5]. In addition, a proportion of elderly normal subjects present with [^{11}C]PiB retention in the neocortex [10–12], suggesting that amyloid PET is potentially useful for presymptomatic detection of Aβ pathology. Although neocortical PiB retention is considered as a high risk for future cognitive decline, not all PiB-positive normal individuals are destined to develop dementia. Some additional biomarkers are thus necessary for accurate prediction of future conversion to dementia. According to previous histopathological study, progression to dementia is associated with a shift from non-fibrillar to fibrillar amyloid deposits in the brain [13]. Thus, selective detection of dense fibrillar amyloid might be advantageous for predicting progression to dementia.

Previously, we had succeeded in developing a unique scaffold of a radioligand, [^{11}C]2-(2-[2-dimethylaminothiazol-5-yl]ethenyl)-6-(2-[fluoro]ethoxy)benzoxazole ([^{11}C]BF-227), as an amyloid imaging probe [3, 14]. Our previous study demonstrated that Aβ deposits in AD patients can be clearly detected by [^{11}C]BF-227 PET [15]. Neocortical [^{11}C]BF-227 retention was further observed in subjects with mild cognitive impairment (MCI) [16]. Using [^{11}C]BF-227 PET, we achieved a sensitivity of 100 % and a specificity of 71.4 % in distinguishing MCI converters to AD from MCI non-converters [17], suggesting the usefulness of this radiotracer for accurate prediction of future progression to dementia. To further take advantage of this imaging potential, especially in a large clinical study, we anticipated that a ^{18}F-labeled derivative of BF-227 would be valuable due to the longer half-life of ^{18}F compared with ^{11}C.

In this study, we performed a biological evaluation of a series of ^{18}F-labeled 2-ethenyl-benzoxazole derivatives (Fig. 1) to select a candidate for clinical application. The one selected, [^{18}F]Fluorinated Amyloid Imaging Compound of Tohoku University ([^{18}F]FACT), was further evaluated for its binding characteristics with Aβ fibrils and plaques and then for its clinical utility as a probe for imaging amyloid in AD.

Methods

Radiosynthesis of ^{18}F-Labeled 2-Ethenyl-Benzoxazole Derivatives

The chemical structures of the 2-ethenyl-benzoxazole derivatives are summarized in Fig. 1. The compounds and their precursors for ^{18}F-labeling were synthesized according to the method described previously [18]. ^{18}F-labeled compounds were prepared according to the following method. The aqueous $^{18}F^-$ contained in K_2CO_3 solution (1.27 to 3.28 GBq) and Kryptofix 2.2.2 were put into a brown vial, and then the water was azeotropically removed with acetonitrile by heating at 110 °C and He-gas flow. After drying, the activated [^{18}F]KF/Kryptofix 2.2.2. was reacted with a tosylate precursor in dimethyl sulfoxide (DMSO) at 110 °C for 10 min, followed by addition of water to quench. The product was extracted by solid-phase extraction with Sep-Pak ^{t}C18 cartridge (Waters) and then eluted with ethanol. The ^{18}F-labeled compound was separated from the eluent by semi-preparative reversed-phase high-performance liquid chromatography (RP-HPLC), isolated from the collected fraction by solid-phase extraction with Sep-Pak ^{t}C18

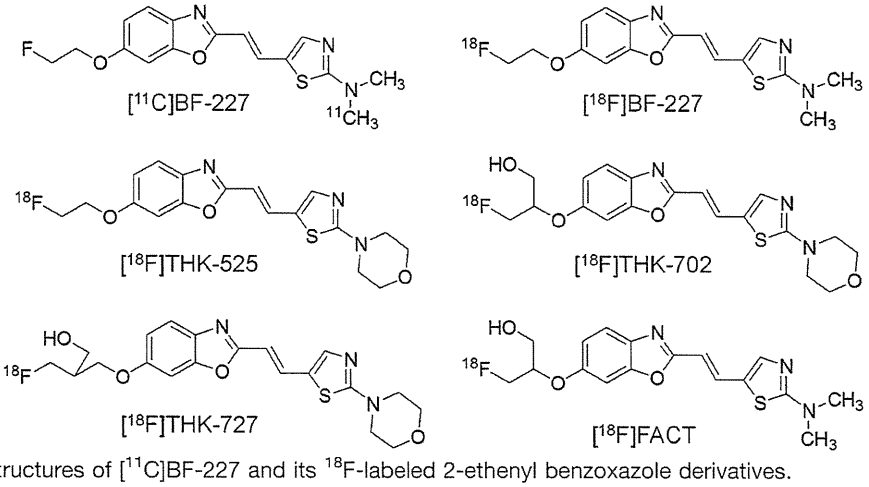

Fig. 1. Chemical structures of [^{11}C]BF-227 and its ^{18}F-labeled 2-ethenyl benzoxazole derivatives.

cartridge, and finally dissolved in DMSO or saline with polysorbate-80 (<0.1 %) for biological evaluation.

[^{11}C]BF-227 was synthesized from the precursor by *N*-methylation with [^{11}C]methyl triflate in DMSO and separated from the crude mixture by semi-preparative RP-HPLC, as described previously [15]. The purified [^{18}F]FACT and [^{11}C]BF-227 were solubilized in isotonic saline containing 1 % polysorbate-80 and 5 % ascorbic acid and then filter-sterilized with 0.22 μm Millipore filter for clinical use.

Fluorescent Staining

Postmortem brain tissue from a 69-year-old man with autopsy-confirmed AD was obtained from Fukushimura Hospital (Toyohashi, Japan). Experiments were performed under the regulations of the hospital ethics committee. Serial sections (6 μm) taken from paraffin-embedded blocks of the temporal cortex were prepared in xylene and ethanol. Before staining with test compounds, quenching of autofluorescence was performed. The quenched tissue section was immersed in 100 μM of test compounds containing 50 % ethanol for 10 min. The stained section was then dipped briefly into water before coverslipping with FluorSave Reagent (Calbiochem, La Jolla, CA, USA) and examination using an Eclipse E800 microscope (Nikon, Tokyo, Japan) equipped with a V-2A filter set (excitation 380 to 420 nm, dichroic mirror 430 nm, long pass filter 450 nm). An adjacent section was immunostained using 4G8 (Signet, Dedham, MA, USA), a monoclonal antibody against Aβ. After pretreatment with 90 % formic acid for 5 min, sections were immersed in blocking solution for 30 min and then incubated for 60 min at 37 °C with 4G8 at a dilution of 1:100. After incubation, sections were processed with biotinylated anti-mouse IgG (Wako) for 60 min, followed by Texas Red-conjugated streptavidin (Vector Laboratories, Burlingame, CA, USA).

In Vitro Autoradiography

A temporal brain section from a 76-year-old female AD patient was incubated with 1.85 MBq/ml of [^{18}F]FACT at room temperature for 20 min and then washed briefly with water and 70 % ethanol. After drying, the labeled section was exposed to a BAS-III imaging plate (Fuji Film, Tokyo, Japan) for 120 min. Autoradiograms were obtained using a BAS-5000 phosphor imaging instrument (Fuji Film, Tokyo, Japan). Neighboring sections were immunostained using 4G8 anti-Aβ monoclonal antibody. After incubation with 4G8, sections were processed by the avidin–biotin method using a Pathostain ABC-POD(M) Kit (Wako, Osaka, Japan) and diaminobenzidine tetrahydrochloride.

In Vitro Binding Study

Amyloid β_{1-40} (Peptide Institute, Inc., Japan) was dissolved in 50 mM potassium phosphate buffer (pH 7.4) to a final concentration of 20 μM. To prepare amyloid fibrils, the solution was incubated at 37 °C for 4 days at 85 rpm and then sonicated to obtain a uniform suspension. The fibril solution was diluted to 2 μM with phosphate-buffered saline (PBS) containing 0.1 % bovine serum albumin (BSA). For saturation binding assay, 100 μl of the fibril solution was mixed with [^{18}F]FACT solution (0.2 to 800 nM, PBS containing 0.1 % BSA and 2 % DMSO, 100 μl) in a 96-well plate. Non-specific binding was defined in the presence of 2 μM FACT in the final solution. The mixture was incubated for 40 min at room temperature and then was passed through the glass filter plate under vacuum with MultiScreen HTS Vacuum Manifold (Millipore Corp., USA), followed by washing with PBS containing 0.1 % BSA twice. Radioactivity of the filter was counted with an automatic gamma counter. The binding data were analyzed with curve-fitting software that calculates the K_d and B_{max} using non-linear regression (GraphPad Prism Version 5.0, GraphPad Software, San Diego, CA, USA).

Biodistribution Study in Normal Mice

The experimental protocols were reviewed by the Committee on the Ethics of Animal Experiments at Tohoku University School of Medicine and performed in accordance with the Guidelines for Animal Experiments issued by the Tohoku University School of Medicine. Male Crj:CD-1 (ICR) mice (6 weeks old, 25 to 30 g, n=12) were injected in a lateral tail vein with ^{18}F-labeled test compounds (370 to 740 kBq) contained in isotonic saline (0.2 ml). The mice were sacrificed by cervical dislocation following heart puncture to obtain blood samples at 2, 30, and 60 min postinjection (n=4 at each time point). Tissues of interest were excised and weighed, and the radioactivity was counted in an automatic gamma-counter. Radioactivity uptake data are expressed as percent of injected dose per gram of tissue (%ID/g).

Autoradiography of Aβ Deposits in Living Transgenic Mice

An amyloid precursor protein (APP) transgenic (Tg) mouse (female, 31 months old) and a wild-type littermate (female, 31 months old) were injected with [^{18}F]FACT (37 MBq) *via* tail vein. The mice were sacrificed by cervical dislocation at 2 h postinjection, and the brains were rapidly excised and frozen in liquid nitrogen. Frozen sections of 20 μm thick were prepared from the brains for *ex vivo* autoradiography. Autoradiograms were obtained in the same manner described above. The sections used for autoradiography were then subjected to fluorescent staining with thioflavin-S according to the previously described method [19].

Clinical PET Study Using [^{18}F]FACT

Ten patients with amnestic MCI, ten patients with AD, and ten normal age-matched controls participated in the clinical PET study using [^{18}F]FACT. Please refer to Table 1 for characteristics of participants. [^{11}C]BF-227 PET scan was additionally performed in two patients with AD (70-year-old woman (MMSE score 17) and 79-year-old man (MMSE score 20)) and 1 normal control subject (60-year-old man (MMSE score 30)). The average time interval between [^{18}F]FACT and [^{11}C]BF-227 PET scans was 12±6 months. Diagnosis of probable AD was based on criteria from the National Institute of Neurological and Communicative Disorders and Stroke and the Alzheimer's Disease Related Disorders Association [20]. The diagnosis of amnestic MCI was made according to published criteria described previously [21]. The control subjects were

Table 1. Subject and patient demographics in [^{18}F]FACT PET comparisons

	NC	MCI	AD
N	10	10	10
Gender (F/M)	4/6	7/3	7/3
Age (years)	69.8±8.8 (60–89)	74.2±8.8 (57–89)	74.5±4.6 (66–81)
MMSE score	29.9±0.3 (29–30)	26.4±1.1 (24–28)	19.8±3.0 (15–24)

recruited from volunteers who were taking no centrally acting medications, had no cognitive impairment, and had no cerebrovascular lesions, including asymptomatic cerebral infarction on T2-weighted studies, identified *via* MRI. All volunteers were screened using a questionnaire and medical history, and those with medical conditions potentially affecting the central nervous system were excluded. The Committee on Clinical Investigation at Tohoku University School of Medicine and the Advisory Committee on Radioactive Substances at Tohoku University approved the study protocol. After complete description of the study to the patients and subjects, written informed consent was obtained.

Image Acquisition Protocols

[^{18}F]FACT-PET and [^{11}C]BF-227-PET study was performed using a SET-2400W PET scanner (Shimadzu, Kyoto, Japan). After intravenous injection of 111–185 MBq of [^{18}F]FACT or 211–366 MBq of [^{11}C]BF-227, dynamic PET images were obtained for 60 min (23 sequential scans; 5 scans×30 s, 5 scans×60 s, 5 scans×150 s, and 8 scans×300 s) with the subject's eyes closed. SUV summation images at 0–10, 10–20, 20–30, 30–40, 40–50, and 50–60 min postinjection were created for the analysis of tracer uptake. T1-weighted MR images were obtained using a SIGNA 1.5 T machine (General Electric, Milwaukee, WI, USA).

Image Analysis

Firstly, standardized uptake value (SUV) images of [^{18}F]FACT and [^{11}C]BF-227 were obtained by normalizing tissue radioactivity concentration by injected dose and body weight. Subsequently, individual MR images were anatomically coregistered into individual PET images using Statistical Parametric Mapping software (SPM5: Welcome Department, UK). Regions of interest (ROIs) were placed on individual axial MR images in the cerebellar hemisphere, frontal cortex [Brodmann's areas (BA) 8, 9, 10, 44, 45, 46, and 47], lateral temporal cortex (BA 21, 22, 37, and 38), parietal cortex (BA 39 and 40), occipital cortex (BA 17), anterior cingulate cortex, posterior cingulate cortex, medial temporal cortex (BA 27, 28, 34, and 35), striatum, pons, and subcortical white matter, as described previously [15]. The ROI information was then copied onto dynamic PET SUV images, and regional SUVs were sampled using PMOD software (PMOD Technologies, Ltd., Zurich, Switzerland). The ratio of regional SUV to cerebellar SUV (SUVR) was calculated as an index of tracer retention. Averaged SUVR in the frontal, temporal, parietal, and posterior cingulate cortices was considered representative of tracer retention in the neocortex (neocortical SUVR). The inter-rater reliability for the ROI measurement was tested between two raters (N.O. and K.S.) in seven subjects and patients. The intra-class correlation coefficient was 0.95.

Statistical Analysis

For statistical comparison in the three groups, we applied the Kruskal–Wallis test followed by Dunn's multiple comparison test. Differences of time activity curves (TACs) in [^{18}F]FACT PET were also evaluated by repeated measures ANOVA followed by the Bonferroni–Dunn post hoc test. For statistical comparisons of PET measurements in control and AD groups, we used the Mann–Whitney *U* test. Effect size coefficients (Cohen's *d*) were also calculated for the evaluation of group differences in PET measurements. Statistical significance for each analysis was defined as $P<0.05$. Correlations between [^{18}F]FACT and [^{11}C]BF-227 SUVR in the frontal, temporal, parietal, and occipital cortices of three subjects (two AD and one normal control) were determined using Pearson's correlations. A linear model was applied to the data to obtain a correlation coefficient and *p* value. These analyses were performed using GraphPad Prism5 software (GraphPad, San Diego, CA, USA).

Results

Radiosynthesis

^{18}F-labeled 2-ethenyl-benzoxazole derivatives (Fig. 1) were obtained in yields of 32 % on average (21 to 44 %, decay-corrected) with radiochemical purity greater than 99 % after HPLC purification. The specific activities ranged 70 to 180 GBq/μmol, corrected at the end of synthesis.

In Vitro Binding to Aβ Plaques in AD Brain Sections

Binding ability of 2-ethenyl-benzoxazole derivatives to Aβ plaques was examined using AD brain sections from a 69-year-old man with autopsy-confirmed AD. As shown in Fig. 2a, c, dense cored plaques (arrowheads) were clearly stained with FACT. In particular, Aβ plaque cores were brightly stained with this compound. The fluorescent staining pattern of FACT correlated well with Aβ immunostaining (Fig. 2b) and thioflavin-S staining (Fig. 2d) in adjacent sections. Other compounds produced similar results in the histopathological staining of AD brain sections from a 69-year-old man with autopsy-confirmed AD.

In vitro autoradiography at tracer dose indicated [^{18}F]FACT binding to dense Aβ deposits (arrowheads) in AD temporal brain sections from a 76-year-old female AD patient (Fig. 2e–h). Tracer signals were additionally detected

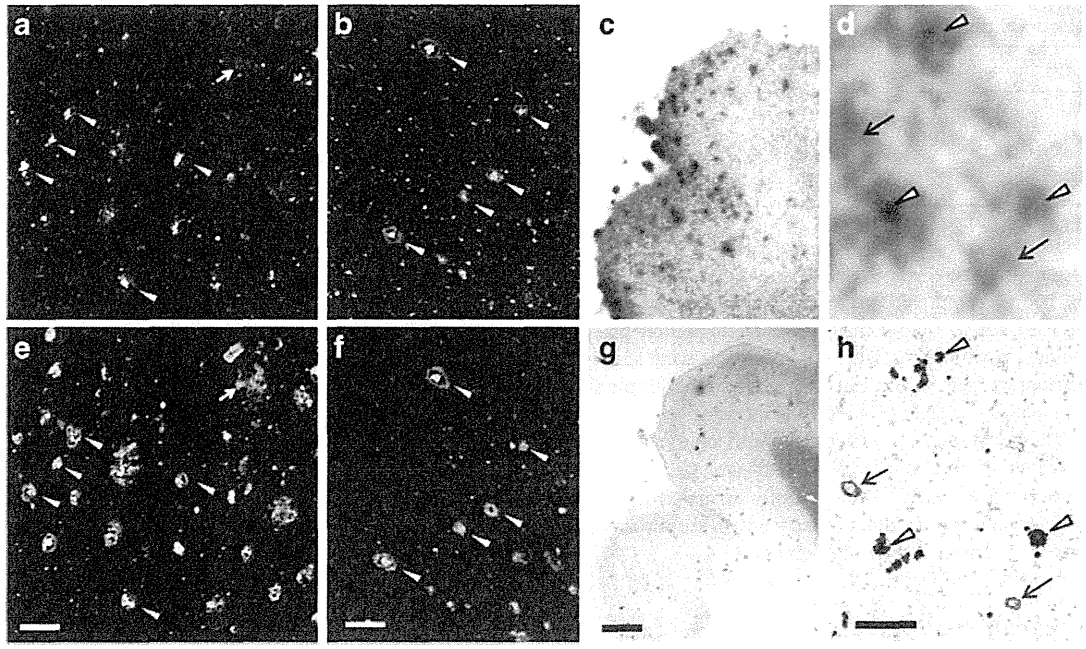

Fig. 2. **a–d** Fluorescence microscopy images of AD brain sections from a 69-year-old man with autopsy-confirmed AD stained with FACT (**a**, **c**), anti-Aβ (4 G8) antibody (**b**), and thioflavin-S (**d**). *Arrowheads* delineate dense cored plaques, respectively. **e–h** Autoradiogram of AD brain section from a 76-year-old female AD patient with [^{18}F]FACT (**e**, **g**) and images of the adjacent section immunostained with anti-Aβ (4 G8) antibody (**f**, **h**). *Arrows* and *arrowheads* delineate congophilic amyloid angiopathy and dense cored plaques, respectively. *Bars* 100 μm (**a–d**), 2 mm (**e–f**), 200 μm (**g–h**).

in congophilic amyloid angiopathy (arrows). These results indicated that FACT and its derivatives had an ability to detect pathological dense Aβ deposits in AD brain tissue.

Binding Affinity to Synthetic Aβ Fibrils

Binding properties of [^{18}F]FACT with Aβ fibrils were investigated by *in vitro* binding assay. Scatchard analysis of FACT binding to Aβ fibrils showed two classes of binding sites: a high-affinity site (K_d=9.4 nM; B_{max}= 0.16 pmol/nmol of Aβ) and a low-affinity site (K_d= 263 nM; B_{max}=1.52 pmol/nmol of Aβ).

Biodistribution Study in Normal Mice

Two important properties of an amyloid imaging probe are rapid brain uptake and rapid clearance from the normal brain without non-specific binding. These properties of the ^{18}F-labeled 2-ethenyl-benzoxazole derivatives were evaluated by biodistribution studies in 12 normal mice (n=4 at each time point). The radioactivity uptake in the blood, brain, liver, kidney, and bone is summarized in Table 2. Regarding brain uptake, all of the ^{18}F-labeled derivatives showed rapid and sufficient brain uptake (4 to 6 %ID/g at 2 min) and smooth washout after that. However, the brain uptake at 60 min varied from 0.28 to 1.68 %ID/g, suggesting a different clearance property in normal brain. Among the derivatives, [^{18}F]FACT indicated the highest ratio of brain uptakes at 2 min to that at 60 min (4.64/0.28=16.6). Additionally, mice injected with [^{18}F]FACT exhibited no increase of the radioactivity uptake in bone with time, unlike with [^{18}F]BF-227, suggesting that [^{18}F] FACT has good stability in regard to metabolic defluorination *in vivo*. Thus, we selected [^{18}F]FACT as the candidate for the clinical comparisons.

Autoradiography of Aβ Deposits in Living Transgenic Mouse

In vivo binding ability of [^{18}F]FACT with amyloid plaques was evaluated in the APP-Tg mouse. Autoradiographic images of the APP-Tg mouse brain post-intravenous injection of [^{18}F]FACT displayed high uptake of the labeling compound in the cortex and hippocampus (Fig. 3a). In contrast, no notable binding was observed in the brain of wild-type mouse (Fig. 3b). These [^{18}F]FACT binding results in APP-Tg mouse brain corresponded closely with those of *in vitro* thioflavin-S staining in the same brain sections (Fig. 3c, d). These results warranted further clinical investigation of [^{18}F]FACT PET in AD patients.

Clinical PET Study Using [^{18}F]FACT

Demographic data for the participants are summarized in Table 1. No statistical difference in age was observed among the three groups. MCI and AD patients had significantly lower mean MMSE scores than normal controls (P<0.05,

Table 2. Biodistribution of ^{18}F-labeled compounds in mice

Tracers	Time (min)	Radioactivity uptakes (%ID/g)				
		Blood	Brain	Liver	Kidney	Bone
[^{18}F]BF-227	2	2.93±0.08	6.05±0.45	7.97±1.59	9.63±0.89	1.59±0.27
	30	2.14±0.17	1.91±0.05	5.75±0.42	3.04±0.15	4.38±1.24
	60	2.09±0.15	1.67±0.14	5.48±0.23	2.42±0.20	7.04±0.75
[^{18}F]THK-525	2	2.82±0.38	4.73±1.32	5.93±1.40	7.72±2.44	1.77±0.87
	30	2.20±0.24	2.05±0.16	3.55±0.60	2.32±0.18	6.74±2.20
	60	1.91±0.29	1.68±0.15	2.47±0.23	1.48±0.14	9.65±0.89
[^{18}F]THK-702	2	3.34±0.13	4.15±0.28	7.53±0.50	13.6±0.88	1.95±0.34
	30	1.06±0.19	0.53±0.03	4.55±0.39	1.58±0.64	0.92±0.11
	60	0.67±0.08	0.35±0.04	3.65±0.72	0.65±0.09	1.16±0.70
[^{18}F]THK-727	2	2.94±0.33	4.06±0.26	9.89±4.16	11.4±1.35	2.08±0.39
	30	1.52±0.10	1.04±0.08	6.68±1.22	2.47±0.36	6.61±0.79
	60	0.66±0.10	0.69±0.02	4.04±1.87	0.98±0.14	9.33±1.34
[^{18}F]FACT	2	3.65±0.66	4.64±0.55	9.38±0.43	10.2±1.05	1.84±0.18
	30	1.19±0.49	0.53±0.11	11.3±1.32	4.17±0.44	0.88±0.07
	60	0.64±0.13	0.28±0.04	14.1±0.55	3.25±0.27	1.38±0.46

Data are expressed as mean±SD (n=4 at each time point)

Kruskal–Wallis test). AD patients additionally had significantly lower mean MMSE scores than those with MCI ($P<$ 0.05, Kruskal–Wallis test). No toxic events were observed in the current clinical trial. The SUV-TACs from [^{18}F]FACT-PET in AD patients and normal control subjects are shown in Fig. 4. Both groups showed rapid entry of [^{18}F]FACT into the neocortex and cerebellum. In the AD patients, the temporal cortex, known to contain high concentrations of fibrillar amyloid plaques in AD, showed retention of [^{18}F] FACT during the later time points compared with the cerebellum (Fig. 4a). In contrast, TACs in the temporal cortex and the cerebellum were nearly identical in normal subjects (Fig. 4b). The subcortical white matter regions showed relatively lower entry and slower clearance than gray matter areas, but no difference in TACs between AD patients and normal controls.

SUVR in the lateral temporal cortex of AD patients was significantly higher over 10 min postinjection of [^{18}F]FACT than those of normal controls ($p<0.05$, Mann–Whitney U test) and reached maximum value at 30 to 40 min postinjection (Fig. 4c). Effect size between AD and normal controls showed the highest value at 30 to 40 min postinjection of [^{18}F]FACT (Table 3). The ratio of SUVR in AD to SUVR in normal controls became constant after

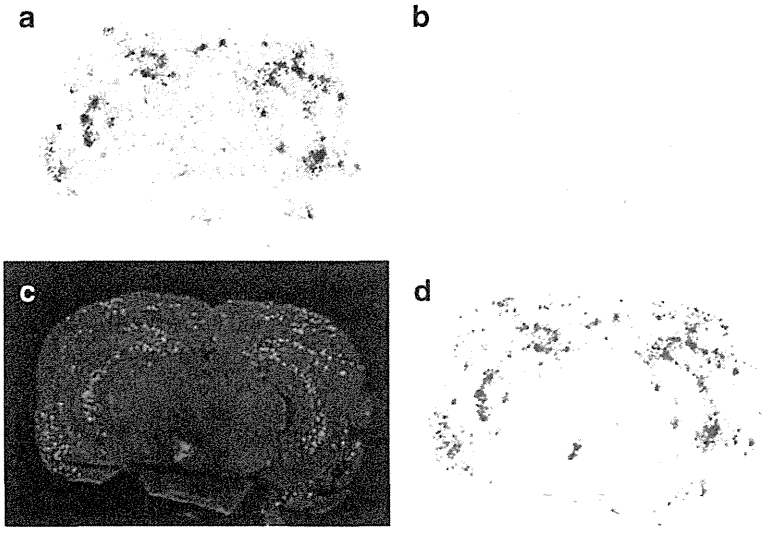

Fig. 3. *Ex vivo* autoradiograms of brain sections from APP transgenic (Tg) mouse (**a**) and wild type mouse (**b**). The brains were excised at 2 h after intravenous injection of [^{18}F]FACT. Aβ plaques in APP-Tg mouse brain were clearly stained with thioflavin-S (**c**). A merged image of **a** and **c** is shown in **d**.

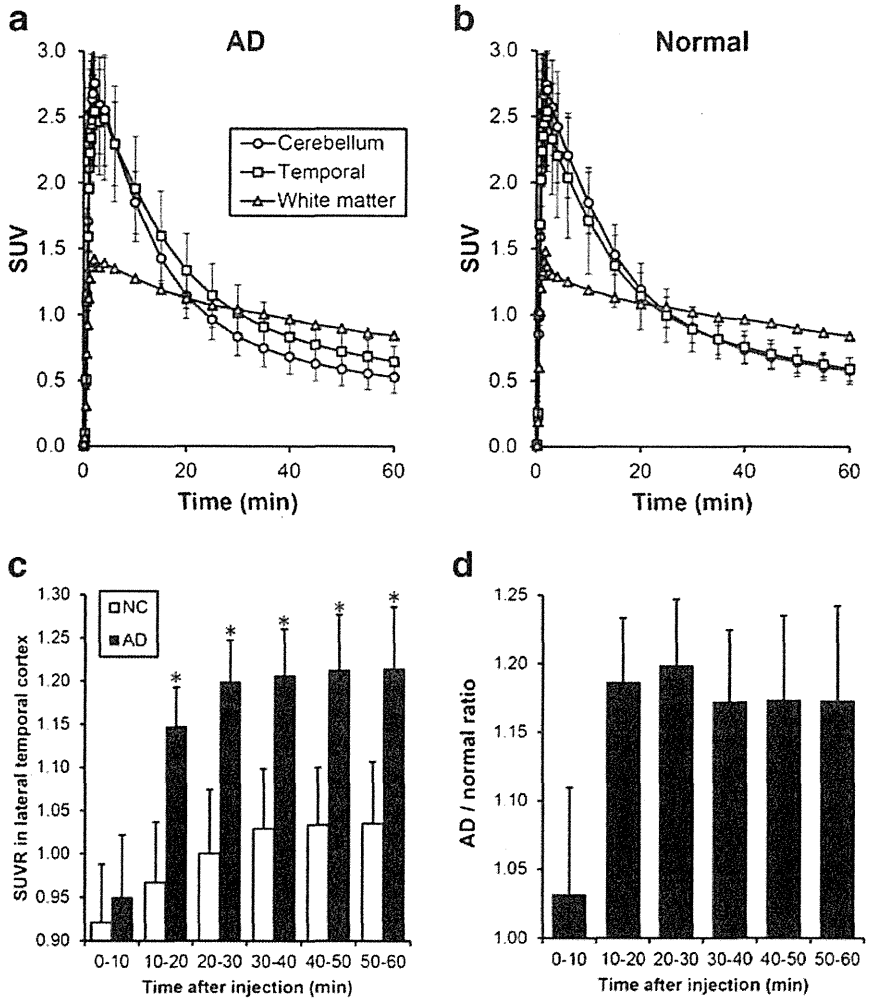

Fig. 4. Time activity data for [^{18}F]FACT PET in humans. Time activity curves of [^{18}F]FACT in ten AD patients (**a**) and ten normal controls (**b**) are shown. Each point represents the mean±standard deviations of data. Time course of [^{18}F]FACT SUVR in the lateral temporal cortex (**c**) and AD *vs* normal ratio of SUVR in the lateral temporal cortex (**d**) are also shown. *P<0.05 by the Mann–Whitney U test.

30 min (Fig. 4d). Based on these results, we selected summed dynamic images from 30 to 40 min for the ROI analysis of PET data.

SUVR images of [^{18}F]FACT for a normal control subject (a 60-year-old man, MMSE score 30) and an AD patient (70-year-old woman, MMSE score 17) are shown in Fig. 5a. Cortical retention of [^{18}F]FACT at 30 to 40 min postinjection was evident in the AD patient, as contrasted with the images of the normal control subject. This pattern of distribution was consistent with the distribution of [^{11}C]BF-227 at 30 to 40 min postinjection in the same subject and patient pair (Fig. 5a). The SUV-TACs from [^{18}F]FACT-PET were compared with those from [^{11}C]BF227-PET in the same AD patient (70-year-old woman, MMSE score 17). As shown in Fig. 5b, [^{18}F]FACT showed faster washout from both temporal cortex and cerebellum than [^{11}C]BF-227. The regional SUVR of [^{18}F]FACT at 30 to 40 min postinjection was compared with that of [^{11}C]BF-227 at the same time frame. SUVR values in the frontal, temporal, parietal, and occipital cortices of three subjects (two AD and one normal control) were used for this analysis. As shown in Fig. 5c, regional SUVR of [^{18}F]FACT were significantly correlated with that of [^{11}C]BF-227 (Pearson's r= 0.931, P<0.001) in these three subjects.

In the quantitative comparison of regional SUVR 30 to 40 min post-administration, the values for the frontal, lateral

Table 3. Time course of lateral temporal [^{18}F]FACT SUVR and effect size measures in ten normal controls and ten AD patients

Time (min)	Normal control	AD	Cohen's d
30–40	1.07±0.06	1.22±0.05*	2.67
40–50	1.08±0.06	1.23±0.06*	2.37
50–60	1.09±0.06	1.23±0.06*	2.34

*P<0.05 by the Mann–Whitney U test

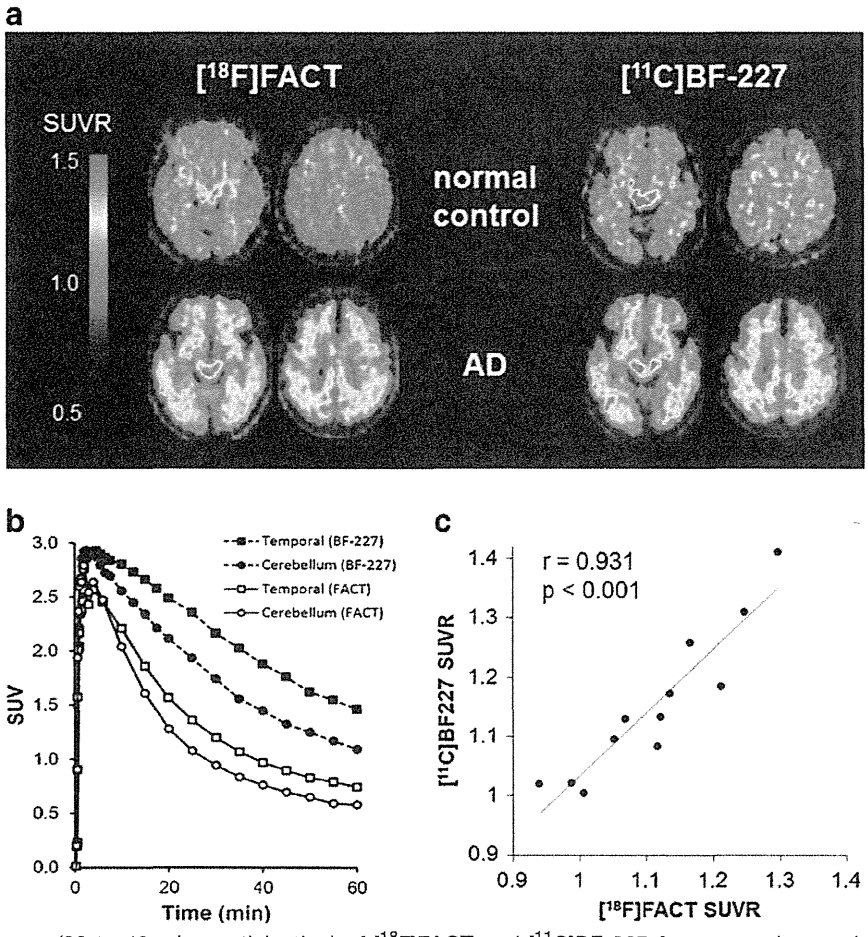

Fig. 5. **a** SUVR images (30 to 40 min postinjection) of [^{18}F]FACT and [^{11}C]BF-227 for a normal control subject (60-year-old man, MMSE score 30) and an AD patient (70-year-old woman, MMSE score 17). **b** Time activity curves of [^{18}F]FACT and [^{11}C]BF-227 in an AD patient (70-year-old woman, MMSE score 17). **c** Significant correlation between regional SUVR of [^{18}F]FACT and [^{11}C]BF-227 in two AD (70-year-old woman (MMSE score 17) and 79-year-old man (MMSE score 20)) and one normal control (60-year-old man, MMSE score 30) subjects (Pearson's r=0.931, P<0.001).

temporal, parietal, occipital, and anterior and posterior cingulate cortices were significantly greater in AD patients than in the normal controls (Table 4). In addition, the SUVRs for the lateral temporal, parietal, occipital, and anterior and posterior cingulate cortices were significantly greater in AD patients than in those with MCI. As shown in Fig. 6, averaged neocortical SUVR was also significantly greater in AD patients than in normal control subjects and MCI (P<0.05, Kruskal–Wallis test). MCI patients additionally showed significantly greater SUVR in the lateral temporal and frontal cortices than normal subjects, but not significant in other brain regions (P<0.05, Kruskal–Wallis

Table 4. Regional SUVR (30 to 40 min postinjection) and effect size measures of [^{18}F]FACT in ten normal controls and ten MCI and ten AD patients

	Normal control	MCI	AD	Cohen's d NC *vs.* AD
Frontal	1.00±0.10	1.09±0.04*	1.15±0.06*	1.82
Lateral temporal	1.05±0.08	1.13±0.06*	1.21±0.05*,**	2.40
Parietal	1.07±0.07	1.13±0.07	1.21±0.08*,**	1.86
Occipital	1.09±0.08	1.07±0.06	1.17±0.05*,**	1.20
Anterior cingulate	1.08±0.07	1.12±0.08	1.21±0.08*,**	1.73
Posterior cingulate	1.15±0.07	1.17±0.06	1.30±0.07*,**	2.14
Medial temporal	1.10±0.05	1.13±0.04	1.15±0.09	0.69
Striatum	1.31±0.11	1.30±0.06	1.35±0.12	0.35
Pons	1.55±0.15	1.57±0.10	1.54±0.09	0.08
White matter	1.50±0.21	1.47±0.11	1.52±0.13	0.12
Neocortex	1.04±0.07	1.12±0.05	1.19±0.05*,**	2.47

*P<0.05 (vs normal control group) and **P<0.05 (vs MCI group) by the Kruskal–Wallis test followed by Dunn's multiple comparison test

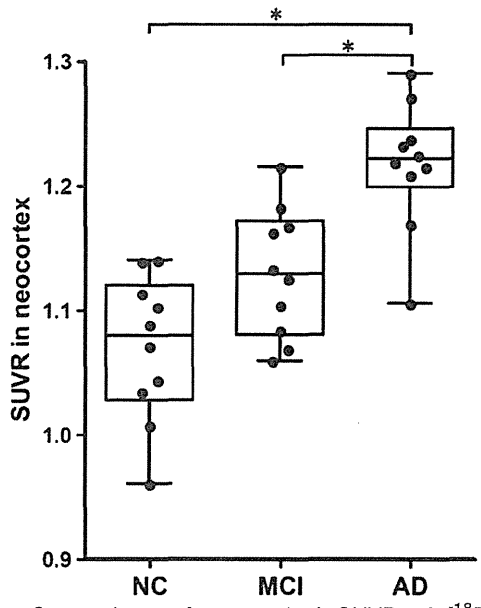

Fig. 6. Comparison of neocortical SUVR of [^{18}F]FACT among ten aged normal controls (NC) and ten mild cognitive impairment (MCI) and ten AD patients. The neocortical SUVRs are represented in a *box* and *whisker plot*. *P<0.05 by the Kruskal–Wallis test followed by Dunn's multiple comparison test.

test). The SUVR in the medial temporal cortex and striatum showed the tendency to be greater in AD patients, but this was not significant. The SUVR in the pons and white matter was nearly identical in AD, MCI, and normal subjects. Effect size value between AD and aged normal subjects was the highest in the lateral temporal cortex (2.40), followed by the posterior cingulate (2.14), parietal (1.86), frontal (1.82), and anterior cingulate (1.73) and occipital (1.20) cortices (Table 4).

Discussion

The current study demonstrated that [^{18}F]FACT PET can be used to detect AD pathology in AD patients and to confirm its absence in cognitively unimpaired elderly people. We previously reported the ability of [^{11}C]BF-227-PET to detect Aβ deposits in the brains of AD patients [15]. The current study has further demonstrated the binding preference of [^{18}F]FACT to dense Aβ plaques in the brains of AD patients. A similar pattern of tracer distribution was observed between [^{18}F]FACT and [^{11}C]BF-227 in AD patients, indicating that [^{18}F]FACT-PET could be substituted for [^{11}C]BF-227-PET for noninvasive detection of dense Aβ deposits in the brain of AD patients. The correlation of [^{18}F]FACT uptake *in vivo* and brain pathology at autopsy should be examined in the future. Our previous studies demonstrated the unique ability of [^{11}C]BF-227 to detect certain forms of prion and α-synuclein protein deposits [22, 23]. Further study will be required to validate the practical usefulness of [^{18}F]FACT-PET for noninvasive detection of these protein deposits.

When a neocortical [^{18}F]FACT SUVR of 1.145 (1.5 SD above control mean) was used as a cutoff, [^{18}F]FACT-PET scan achieved a sensitivity of 90 % (nine of ten) and a specificity of 100 % (ten of ten) in the discrimination between AD patients and normal subjects. In one exception, a 76-year-old female AD patient, MMSE score 24, showed no remarkable retention of [^{18}F]FACT in the neocortex. This is not surprising because approximately 10 to 20 % of patients diagnosed as probable AD reportedly fail to meet pathological criteria for AD at autopsy.

The amnestic subtype of MCI has a high risk of progression to dementia, and it may constitute a prodromal stage of AD [24]. Previous amyloid-PET studies demonstrated a substantial amount of neocortical tracer retention in 50 to 60 % of the MCI population, which is comparable to the level in AD patients [10, 17]. In our study, about half of the MCI patients had elevated neocortical [^{18}F]FACT retention, which was an intermediate level between the aged normal subjects and the AD patients. This finding is in accord with the previous neuropathological observation that the density of neuritic plaque increased as a function of increasing dementia severity [25]. The parent tracer [^{11}C]BF-227 showed neocortical retention to be a reliable indicator of disease progression in MCI subjects in our previous study [17, 19]. Therefore, PET imaging with [^{18}F]FACT is also expected to have a similar prognostic utility.

The amount of elevation of neocortical [^{18}F]FACT uptake in AD patients was approximately 14 to 15 %, far less than PiB and other ^{18}F-labeled amyloid-PET tracers. This is probably due to the relatively low binding affinity and B_{max} of this tracer with amyloid fibrils in comparison to that of PiB (K_d=1.02 nM, B_{max}=0.61) [26, 27]. There is considerable amount of tracer retention in the white matter, which reflects non-specific binding of the compound to myelin sheath. Because of modest specific binding of [^{18}F]FACT in the gray matter of AD patients, spillover from the white matter could reduce the sensitivity for detecting amyloid positive subjects. Use of early phase (30 to 40 min postinjection) images can compensate for this because the relatively stronger signals in the gray matter persist in this time interval. Partial volume correction may also be able to improve the discriminatory power of [^{18}F]FACT-PET by eliminating nonspecific signals in the white matter. Another method to improve the sensitivity for detecting specific signals in the brain is to create a statistical map by comparison with a normal control database [19].

One of advantages of [^{18}F]FACT over BF-227 is its rapid kinetic profile. [^{18}F]FACT showed faster washout from normal brain tissue than BF-227 (Fig. 5) probably because of the lower lipophilicity of FACT (LogP=1.99±0.02) as compared to BF-227 (LogP=2.29±0.02). The neocortical SUVR of [^{18}F]FACT reached a peak at 30 min post-administration. This characteristic would also contribute to reduced procedure and waiting times for PET scans.

Conclusion

We successfully developed a novel ^{18}F-labeled ethenylbenzoxazole derivative, [^{18}F]FACT, as a PET tracer for amyloid deposits. This tracer preferentially bound to dense Aβ plaques in AD brain sections, visualized cortical amyloid deposits in APP Tg mice, and demonstrated fast kinetics and significant retention of [^{18}F]FACT in sites with predilection for the deposition of dense amyloid plaques in AD patients during clinical PET imaging. [^{18}F]FACT PET distinctly distinguished AD patients from normal individuals. These findings suggest that [^{18}F]FACT may be usable for *in vivo* detection of dense Aβ plaques in AD brains.

Acknowledgments. This study was financially supported by the Special Coordination Funds for Promoting Science and Technology, the Health and Labour Sciences Research Grants for Translational research from Ministry of Health, Labour and Welfare, the Program for Promotion of Fundamental Studies in Health Science of the National Institute of Biomedical Innovation, and the Grant-in-Aid for Scientific Research (C) (20591432) from the Ministry of Education, Culture, Sports, Science and Technology of Japan. The authors appreciate the technical assistance of Dr. Shoichi Watanuki in the clinical PET studies.

Conflict of Interest. The authors declare they have no conflicts of interest.

References

1. McKhann GM, Knopman DS, Chertkow H et al (2011) The diagnosis of dementia due to Alzheimer's disease: recommendations from the National Institute on Aging—Alzheimer's Association workgroups on diagnostic guidelines for Alzheimer's disease. Alzheimers Dement 7:263–269
2. Kadir A, Nordberg A (2010) Target-specific PET probes for neurodegenerative disorders related to dementia. J Nucl Med Off Publ Soc Nucl Med 51:1418–1430
3. Furumoto S, Okamura N, Iwata R, Yanai K, Arai H, Kudo Y (2007) Recent advances in the development of amyloid imaging agents. Curr Top Med Chem 7:1773–1789
4. Okamura N, Fodero-Tavoletti MT, Kudo Y et al (2009) Advances in molecular imaging for the diagnosis of dementia. Expert Opin Med Diagn 3:705–716
5. Klunk WE, Engler H, Nordberg A et al (2004) Imaging brain amyloid in Alzheimer's disease with Pittsburgh Compound-B. Ann Neurol 55:306–319
6. Vandenberghe R, Van Laere K, Ivanoiu A et al (2010) ^{18}F-flutemetamol amyloid imaging in Alzheimer disease and mild cognitive impairment: a phase 2 trial. Ann Neurol 68:319–329
7. Barthel H, Gertz HJ, Dresel S et al (2011) Cerebral amyloid-beta PET with florbetaben (^{18}F) in patients with Alzheimer's disease and healthy controls: a multicentre phase 2 diagnostic study. Lancet Neurol 10:424–435
8. Clark CM, Schneider JA, Bedell BJ et al (2011) Use of florbetapir-PET for imaging beta-amyloid pathology. Jama 305:275–283
9. Jureus A, Swahn BM, Sandell J et al (2010) Characterization of AZD4694, a novel fluorinated Abeta plaque neuroimaging PET radioligand. J Neurochem 114:784–794
10. Rowe CC, Ng S, Ackermann U et al (2007) Imaging beta-amyloid burden in aging and dementia. Neurology 68:1718–1725
11. Hatashita S, Yamasaki H (2010) Clinically different stages of Alzheimer's disease associated by amyloid deposition with [^{11}C]-PIB PET imaging. J Alzheimer's Dis JAD 21:995–1003
12. Villemagne VL, Pike KE, Chetelat G et al (2011) Longitudinal assessment of Abeta and cognition in aging and Alzheimer disease. Ann Neurol 69:181–192
13. Dickson TC, Vickers JC (2001) The morphological phenotype of beta-amyloid plaques and associated neuritic changes in Alzheimer's disease. Neuroscience 105:99–107
14. Okamura N, Suemoto T, Shimadzu H et al (2004) Styrylbenzoxazole derivatives for *in vivo* imaging of amyloid plaques in the brain. J Neurosci 24:2535–2541
15. Kudo Y, Okamura N, Furumoto S et al (2007) 2-(2-[2-Dimethylaminothiazol-5-yl]ethenyl)-6- (2-[fluoro]ethoxy)benzoxazole: a novel PET agent for *in vivo* detection of dense amyloid plaques in Alzheimer's disease patients. J Nucl Med 48:553–561
16. Barthel H, Luthardt J, Becker G et al (2011) Individualized quantification of brain beta-amyloid burden: results of a proof of mechanism phase 0 florbetaben PET trial in patients with Alzheimer's disease and healthy controls. Eur J Nucl Med Mol Imaging 38:1702–1714
17. Waragai M, Okamura N, Furukawa K et al (2009) Comparison study of amyloid PET and voxel-based morphometry analysis in mild cognitive impairment and Alzheimer's disease. J Neurol Sci 285:100–108
18. Kudo Y, Furumoto S, Okamura N (2010) Benzoxazole derivatives. US Patent Application 2010/0021385
19. Shao H, Okamura N, Sugi K et al (2010) Voxel-based analysis of amyloid positron emission tomography probe [^{11}C]BF-227 uptake in mild cognitive impairment and Alzheimer's disease. Dement Geriatr Cogn Disord 30:101–111
20. McKhann G, Drachman D, Folstein M, Katzman R, Price D, Stadlan EM (1984) Clinical diagnosis of Alzheimer's disease: report of the NINCDS-ADRDA Work Group under the auspices of Department of Health and Human Services Task Force on Alzheimer's Disease. Neurology 34:939–944
21. Petersen RC, Smith GE, Waring SC, Ivnik RJ, Tangalos EG, Kokmen E (1999) Mild cognitive impairment: clinical characterization and outcome. Arch Neurol 56:303–308
22. Okamura N, Shiga Y, Furumoto S et al (2009) *In vivo* detection of prion amyloid plaques using [^{11}C]BF-227 PET. Eur J Nucl Med Mol Imaging 37:934–941
23. Kikuchi A, Takeda A, Okamura N et al (2010) *In vivo* visualization of alpha-synuclein deposition by carbon-11-labelled 2-[2-(2-dimethylaminothiazol-5-yl)ethenyl]-6-[2-(fluoro)ethoxy]benzoxazole positron emission tomography in multiple system atrophy. Brain J Neurol 133:1772–1778
24. Gauthier S, Reisberg B, Zaudig M et al (2006) Mild cognitive impairment. Lancet 367:1262–1270
25. Haroutunian V, Perl DP, Purohit DP et al (1998) Regional distribution of neuritic plaques in the nondemented elderly and subjects with very mild Alzheimer disease. Arch Neurol 55:1185–1191
26. Fodero-Tavoletti MT, Mulligan RS, Okamura N et al (2009) *In vitro* characterisation of BF227 binding to alpha-synuclein/Lewy bodies. Eur J Pharmacol 617:54–58
27. Fodero-Tavoletti MT, Smith DP, McLean CA et al (2007) *In vitro* characterization of Pittsburgh compound-B binding to Lewy bodies. J Neurosci Off J Soc Neurosci 27:10365–10371